University of Nebraska - Lincoln

DigitalCommons@University of Nebraska - Lincoln

US Army Research

U.S. Department of Defense

2015

Capturing the effects of free surfaces on void strengthening with dislocation dynamics

Joshua C. Crone
U.S. Army Research Laboratory, Aberdeen Proving Ground, MD

Lynn B. Munday
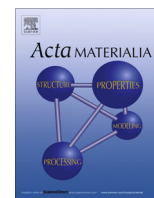*U.S. Army Research Laboratory, Aberdeen Proving Ground, MD*

Jaroslaw Knap
U.S. Army Research Laboratory, Aberdeen Proving Ground, MD

Follow this and additional works at: http://digitalcommons.unl.edu/usarmyresearch

Crone, Joshua C.; Munday, Lynn B.; and Knap, Jaroslaw, "Capturing the effects of free surfaces on void strengthening with dislocation dynamics" (2015). *US Army Research*. 318.
http://digitalcommons.unl.edu/usarmyresearch/318

Capturing the effects of free surfaces on void strengthening with dislocation dynamics

Joshua C. Crone *, Lynn B. Munday, Jaroslaw Knap

U.S. Army Research Laboratory, Aberdeen Proving Ground, MD 21005, USA

ABSTRACT

Void strengthening in crystalline materials refers to the increase in yield stress due to the impediment of dislocation motion by voids. Dislocation dynamics (DD) is a modeling method well suited to capture the physics, length scales, and time scales associated with void strengthening. However, previous DD simulation of dislocation–void interactions have been unable to accurately account for the strong image forces acting on the dislocation due to the void's free surface. In this article, we employ a finite-element-based DD method to determine the obstacle strength of voids, defined as the critical resolved shear stress for a dislocation to glide past an array of voids. Our results demonstrate that the attractive image forces between the dislocation and free surface significantly reduce the obstacle strength of voids. Effects of surface mobility and stress concentrations around the void are also explored and are shown to have minimal effect on the critical stress. Finally, a new model relating void size and spacing to obstacle strength is proposed.

Published by Elsevier Ltd. on behalf of Acta Materialia Inc.

1. Introduction

The plastic deformation of crystalline materials is primarily governed by the evolution of dislocations. Interactions of dislocations with atomic defects and microstructural features are known to significantly affect dislocation motion, altering the macroscopic mechanical response. Voids, frequently introduced during processing, additive manufacturing, or irradiation, are one such feature that has been found experimentally to increase yield strength with increasing void density [1,2]. The increased yield strength is primarily attributed to the pinning of dislocations at the voids [2]. Consequently, the strength of crystalline material is dependent on the obstacle strength of the void configuration, defined as the magnitude of stress necessary for a dislocation to bypass a void array. Despite the fundamental importance of the above void-strengthening in determining the material response in porous crystals, few accurate models exist.

Several studies of the interaction of dislocations and voids have been carried out by means of molecular dynamics (MD) [3–8]. These studies have provided tremendous insight into bypass mechanisms at the atomic scale, such as glide [3], climb [4], and inertial effects [7]. However, void sizes directly accessible to MD are typically in the range of 1–6 nm, whereas corresponding void sizes found in crystalline materials commonly range from tens of nanometers to microns [9–13]. Furthermore, MD, due to its limitations in the size of the computational domain, can frequently only be applied to modeling a single void in a periodic array of voids. Such an idealized arrangement of voids is unlikely to provide a statistically representative characterization of plasticity in crystals with porosity. Finally, temporal scales characteristic to MD require strain rates on the order of 10^6–10^9 1/s, well outside of the range encountered in typical applications.

In contrast with MD, dislocation dynamics (DD) is a more suitable choice for studying yield strength and early stages of strain hardening at larger length and time scales. DD has been shown capable of capturing the strengthening mechanisms due to interaction of dislocations with other defects [14–16]. However, modeling of voids by means of DD has been challenging due to the need to account for the presence of surfaces. Orowan [17] was the first to explicitly model the interaction of dislocations with other defects, namely impenetrable inclusions where free surfaces are not applicable. Subsequently, Bacon, Kocks, and Scattergood [18] expanded Orowan's model to incorporate dislocation self-interactions. According to this model, the critical resolved shear stress, τ_c, required for an edge dislocation to bypass a periodic array of impenetrable inclusions is given by

$$\tau_c = \frac{\mu b}{2\pi L}\left[\ln\left(\frac{\overline{D}}{b}\right) + \Delta\right] \tag{1}$$

* Corresponding author.
E-mail address: joshua.crone.civ@mail.mil (J.C. Crone).

where μ is the shear modulus, b the magnitude of the Burgers vector, D the void diameter, L the void spacing, $\overline{D} = (D^{-1} + L^{-1})^{-1}$, and $\Delta = 0.7$. Scattergood and Bacon [19] extended this model further, replacing impenetrable inclusions with voids. Their model yielded the same functional form of Eq. (1), albeit with $\Delta = 1.52$. At present, the model of Scattergood and Bacon is widely accepted for modeling of the obstacle strength of voids. However, Scattergood and Bacon openly discuss a number of significant simplifications in their model. First and foremost, the image forces which account for the interaction between the dislocation and the free surface are only accounted for at the dislocation-surface intersection point and are neglected otherwise. Furthermore, the effect of the free surface is approximated by means of the simplified geometry of a half-space. In addition, the applied stress field is assumed to be uniform, ignoring the effect of stress concentrations. Finally, mobility of the dislocation along the void's free surface is modified via a surface energy term without a systematic study of its effect on τ_c.

Before DD can be reliably applied to study large scale void-strengthening effects at high void and dislocation densities, it is important to accurately model the obstacle strength of voids in idealized geometries, such as a periodic array. Therefore, the focus of this article is twofold. First, we re-examine the approximations made by Scattergood and Bacon [19] and determine their effects on τ_c. The development of advanced computational tools for computing image forces with arbitrary geometries [20,21] enables us to improve upon these previous predictions with more accurate treatment of image forces. An understanding of the various approximations is a critical step towards performing large scale studies that are both physically accurate and computationally tractable. Second, using a more accurate treatment of the surface effects, we present a new model for the obstacle strength of voids.

2. Methodology

2.1. Simulation procedure

Modeling of dislocation dynamics (DD) with surface effects is performed by coupling a finite element method (FEM) solver [20,21] to the ParaDiS DD simulator [22] following the methodology of van der Giessen and Needleman [23]. A detailed description of the DD and FEM algorithms can be found in Refs. [22,20], respectively. We briefly discuss the main features specific to modeling dislocation–void interactions.

The focus of this work is to identify the minimum resolved shear stress (τ_c) required for a dislocation to bypass a periodic array of voids. To this end, we follow the model setup of Scattergood and Bacon [19], shown in Fig. 1, where an infinite straight edge dislocation is placed near a 1D array of voids. A shear stress (σ_{xy}^{ext}) is applied to drive the dislocation towards the void array. If an equilibrium configuration exists in which the dislocation remains attached to the void, σ_{xy}^{ext} is increased until the dislocation breaks away and bypasses the void array. τ_c is determined when the value of the σ_{xy}^{ext} to bypass the voids is within 1% of the stress to achieve equilibrium. We assume that a static equilibrium has been reached when the peak of the bowed-out dislocation line has not advanced for at least 10^4 time steps. Simulations with a stricter criteria requiring no advancement for 10^5 time steps show no effect on τ_c.

Peach–Koehler forces are computed on each dislocation segment. The forces include contributions from the externally applied stress (f^{ext}), image stress (f^{img}), and the stress due to all dislocation segments in the system (f^{disl}). The calculation of f^{ext} in previous DD simulations with voids have assumed only a uniform applied stress field [19]. However, under an applied stress, stress concentrations
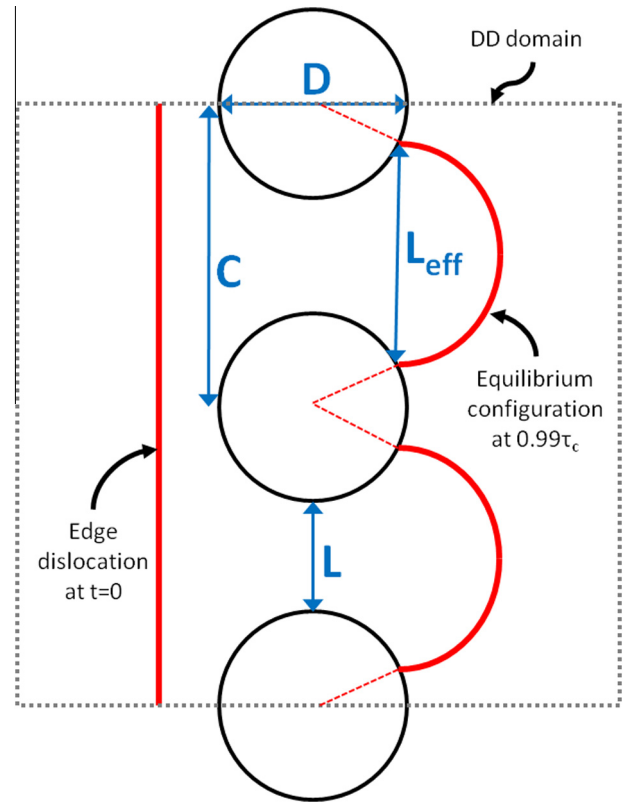

Fig. 1. Schematic of the simulation model setup. Virtual segments are represented by the dotted lines connecting the dislocation line to the center of the voids.

occur around the void and alter the local stress field. In order to determine the effect of these stress concentrations, we compare the results of τ_c using a uniform applied stress to the results explicitly including the stress concentrations. The computation of f^{disl} is performed in ParaDiS using the non-singular dislocation stress field [24] with a core radius of $1b$.

Image forces are required due to the presence of voids and the resulting deviation of dislocation stress field from that in an infinite body. Enforcement of traction free boundary conditions on the surfaces and solving the resulting linear elastic boundary value problem (BVP) provides the corrective image stress field. The image stress is then superimposed with the stress field due to the dislocations in an infinite body [23]. Conservation of the Burgers vector is assured by the introduction of virtual segments [25,20] extending from the surface-piercing dislocations to the center of the void [26] (c.f Fig. 1).

In order to avoid the high computational expense of numerically calculating the image stress field, analytic solutions for the image stress and resulting image force have been developed for some simple geometries. For example, a solution for a straight, semi-infinite dislocation piercing the free surface of a half space was introduced by Lothe [27]. This solution yields a particularly simple dislocation equilibrium condition [19]

$$E\cos(\theta) - E'\sin(\theta) = 0 \qquad (2)$$

where E is the strain energy per unit length of a dislocation, θ is the angle between the dislocation line and the free surface as shown in Fig. 2, and $E' = \partial E/\partial \theta$ is the orientation derivative of E. In Fig. 2b, we illustrate how the left hand side of Eq. (2) can be used to approximate the image forces acting on the dislocation at the surface-dislocation intersection point. Further details on how the Lothe equation is employed to approximate the image forces from a void
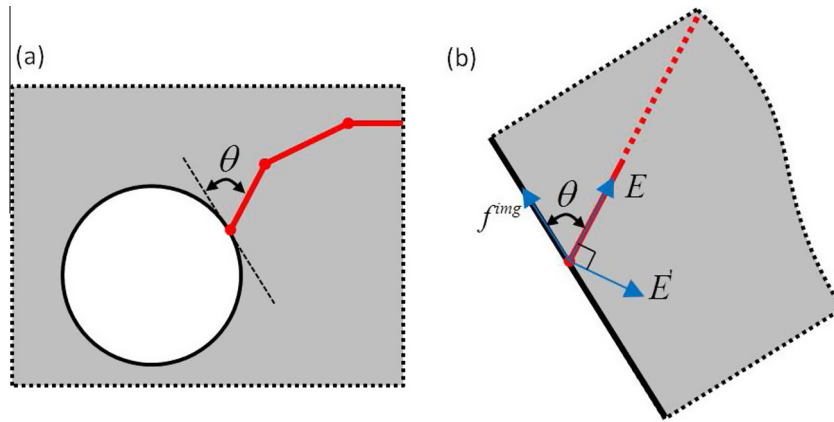
Fig. 2. Illustration of Lothe approximation in which a dislocation line intersecting a void (a) is approximated as a straight, semi-infinite dislocation intersecting a half-space at the same angle with respect to the surface normal (b).

may be found in [19]. We note that when using the Lothe equation, not only is the spherical void surface approximated by a planar half-space, but also the image forces only act where the dislocation intersects the surface. Therefore, the image forces acting on the rest of the dislocation line are ignored. Here, we compare the Lothe approximation to the FEM solution for image stresses, where the latter includes image forces acting on the entire dislocation line. Simulations combining the Lothe and FEM image forces are also performed to demonstrate the benefits of this combined method in resolving the images forces with larger FEM element sizes.

The velocities of the dislocations are computed using a linear mobility of the form $v = B^{-1}f$ where v is the velocity, $f = f^{ext} + f^{img} + f^{disl}$ is the total Peach–Koehler force, and B is the drag coefficient. When seeking equilibrium configurations, B only affects the speed at which the dislocation approaches the equilibrium at $f = 0$. Therefore, we set B equal to the identity matrix for all simulations in this article. Since dislocation motion is limited to the glide plane, climb and cross-slip mechanisms are not considered. Moreover, due to the fact that motion is restricted to a single glide plane, the results are independent of crystal structure. Thus, a simple cubic lattice structure is assumed. The material properties correspond to those of aluminum with shear modulus $\mu = 26.6$ GPa, Poisson's ratio $v = 0.334$, and Burgers vector $b = 2.862$ Å.

Dislocation mobility at the free surface warrants special considerations. In general, lower dislocation mobility is expected at the free surface, as indicated by MD studies [3,28,29]. In order to account for the above effect, we follow Scattergood and Bacon [19] and add an energy barrier to dislocation motion along the surface. The height of this barrier is proportional to the surface energy (γ_s) and corresponds to the resistance experienced by the dislocation from creating a step along the surface. In Scattergood and Bacon, γ_s was varied between 0 and 3 in units of $Gb/4\pi$. In this work, we aim to identify the upper and lower bounds on the effect of γ_s. We first perform simulations with $\gamma_s = 0$, as done in Scattergood and Bacon, to model conditions where there is no added barrier to dislocation glide on the surface. We then perform simulations where the barrier to glide is such that no force can overcome it ($\gamma_s \to \infty$), which is equivalent to pinning the dislocation at the surface intersection point. The latter should provide a more accurate upper bound than the large, but finite, value $\gamma_s = 3Gb/4\pi$ used in Scattergood and Bacon.

2.2. Model geometry

A schematic of the model setup is included in Fig. 1. The model setup consists of three voids equally spaced along the z-axis. Simulations performed with additional voids show no effect on τ_c,

Table 1
Void diameters (D) and center-to-center spacing (C) used throughout this work. Harmonic mean defined as $\bar{D} = DL/(D + L)$ where $L = C - D$.

D [b]	C [b]	C/D	$\bar{D}$ [b]
50	125	2.5	30
50	200	4	37.5
50	400	8	43.75
50	1000	20	47.5
150	375	2.5	90
150	600	4	112.5
150	1200	8	131.25
150	3000	20	142.5
500	1250	2.5	300
500	2000	4	375
500	4000	8	437.5
500	10000	20	475

therefore we treat this configuration as representative of an infinite array. The DD simulation domain is a cube with an edge length twice the center-to-center spacing between voids (C). Periodic boundary conditions are applied along the z-axis as to represent an infinite dislocation approaching an infinite array of voids. The FEM domain is a cube with an edge length of $4C$. Simulations involving larger FEM domains yield no change in the value of τ_c. We note that while our FEM simulations do not include effects from periodic images of the voids, simulations with longer void arrays suggest these effects are not significant. Still, periodic images of the dislocation line are considered during the evaluation of f^{img} and f^{disl}.

Two different void diameters (D) of 50b and 500b are employed to assess the effects of image stress, surface mobility, and stress concentrations in Sections 3.2 and 3.3. The ratios of C/D for these simulations are 2.5 and 20. Additional void sizes and spacings are included in the final set of simulations designed to determine a new model for τ_c in Section 3.4. We list all void configurations in Table 1.

At the onset of the simulation, an edge dislocation is placed at $x = -D$, with a Burgers vector $b = [1\,0\,0]$, line direction $t = [0\,0\,1]$, and glide plane normal $n = [0\,1\,0]$. The dislocation is initially discretized into piecewise linear segments with a minimum segment length of $D/10$. Segments are adaptively remeshed during the course of the simulation as to accurately capture the curvature of the dislocation. The maximum segment length is limited to $\max\{D/5, C/20\}$.

3. Results and discussion

In this section, we present our results in identifying the strengthening effect of voids as obstacles to dislocation glide. First,

we determine the sensitivity of our results to the FEM element size, illustrating the importance of accurately resolving the image stress near the surface. We then determine the effect of multiple approximations in the Scattergood–Bacon model for τ_c. Finally, we propose a new model to determine the critical stress for a dislocation to glide past an array of voids.

3.1. Mesh convergence

When using numerical methods to compute the image stress field, it has been shown that high resolution is required to capture the large stress gradients as dislocations approach the surface [20,30,31,26]. We first examine the convergence in τ_c with respect to FEM element size. Our meshes coarsen away from the void surface, resulting in variable element sizes across the simulation domain. Therefore, we take the element size on the void surface (h) as our indicator of element size for a given mesh. The coarsest mesh size is $h/D = 0.2$. Higher resolution meshes are obtained through global subdivision in which the size of all elements is reduced by a factor of 2. All meshes considered here contain quadratic tetrahedral elements.

Mesh convergence studies have been performed for multiple void configurations in Table 1. However we focus on the configuration of $D = 50b$, $C = 1000b$, which has demonstrated the highest sensitivity with respect to the mesh size. The red squares in Fig. 3 illustrate the convergence of τ_c with respect to h using FEM to compute image forces. We observe that for $h/D \leqslant 0.1$ each subsequent mesh subdivision increases τ_c by less than 2%, indicating the results are relatively insensitive to the mesh size. In contrast, for $h/D = 0.2$, τ_c is significantly underestimated, indicative of strong mesh sensitivity in this range. Given that D is only $50b$ in this simulation, these findings suggest that element sizes on the order of b are required to achieve converged results. With DD simulation sizes often on the order of $10^3 b$ to $10^4 b$, this presents a large computational challenge for accurately capturing image forces.

The sensitivity of τ_c with respect to mesh size observed in Fig. 3 is due to the inability of the FEM mesh to resolve the large gradients of the image stress field at the surface. In an attempt to reduce this sensitivity, we combine the image forces computed from FEM with the image force determined through the Lothe approximation at the surface-dislocation intersection point. We plot the mesh sensitivity for this combined approach represented as the blue

triangles in Fig. 3. A significant reduction in the mesh sensitivity can be observed as the difference in τ_c over three mesh subdivisions from $h/D = 0.2$ to $h/D = 0.025$ is less than 3%. Furthermore, the converged value of 14.55 MPa appears to be in excellent agreement with the results of the highest resolution mesh using only FEM to compute image forces. In all void configurations we examined, the combined method of FEM and Lothe provided the same converged value of τ_c and exhibited lower mesh sensitivity. Thus, the combined approach achieves higher accuracy in the image force calculation with lower mesh resolution and reduced computational expense. We emphasize that this equivalence has only been confirmed for quasistatic simulations to determine equilibrium configurations. The image forces on the surface-intersecting dislocation node is included twice with this combined method. The consistency in the resulting τ_c between the FEM-only and combined methods suggests that both forces are acting towards the same equilibrium configuration and the magnitude of the force may not play an important role. Still, such behavior may not hold true for dynamic simulations or cases where the force magnitude determines events such as cross-slip, climb, or junction formation. In all of the following simulations, $h/D = 0.1$ and references to the FEM method of image force calculation refer to the combined method of FEM with Lothe, unless noted otherwise.

3.2. Image stress and surface mobility

The two primary approximations made in the Scattergood–Bacon model are the Lothe approximation to represent image forces and the arbitrary surface energy term to restrict motion of the dislocation on the surface. In this section, we assess the effects of these approximations on τ_c. The applied stress is still assumed to be uniform, as the effect of stress concentrations is explored later.

The first comparison is between the Lothe approximation and FEM with no modification to the surface mobility ($\gamma_s = 0$). The solid red symbols in Fig. 4 indicate that for all four void configurations the Lothe equation overestimates τ_c by approximately 20%. We note that while no equations or tabulated values are provided by Scattergood and Bacon [19] for τ_c when $\gamma_s = 0$, our results show good qualitative agreement with the results plotted in Ref. [19] with $\gamma_s = 0$.
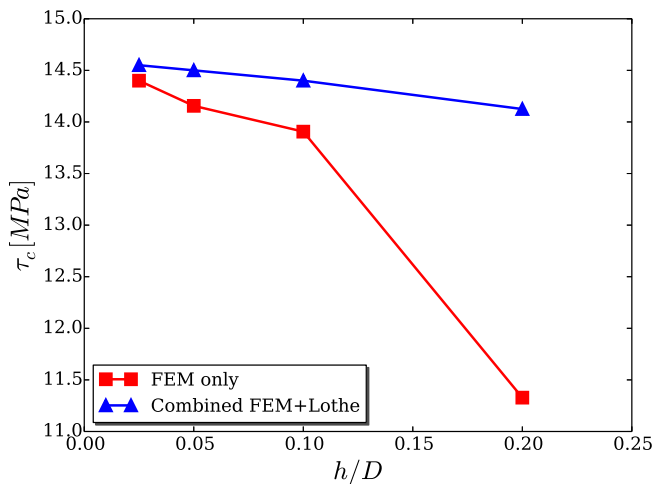

Fig. 3. Convergence of τ_c with respect to FEM element size on the void's surface (h) for void configuration $D = 50b$, $C = 1000b$. The applied stress is uniform and dislocation are free to glide along the surface ($\gamma_s = 0$).
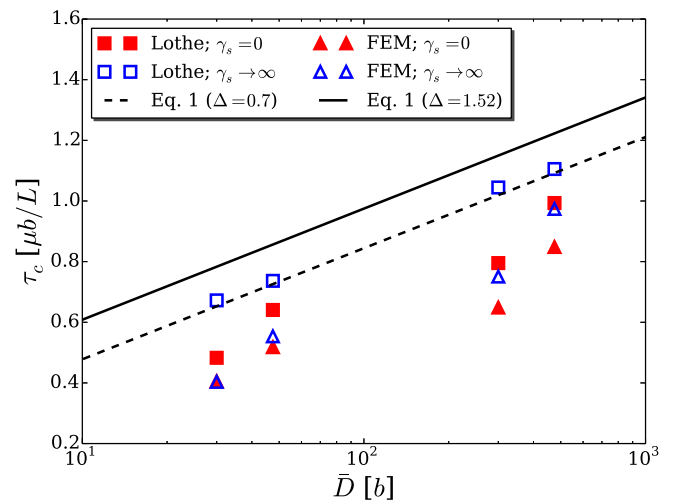

Fig. 4. Normalized τ_c as a function of void size and spacing illustrating the effect of image force calculation method (Lothe vs. FEM) and surface mobility (unrestricted/$\gamma_s = 0$ vs. pinned/$\gamma_s \to \infty$). The straight lines represent Eq. (1) with the values of the fitted coefficient Δ indicated in the legend. Uniform applied stress is used in all simulations.

Comparing the data represented by the empty squares and triangles, we see the effect of image force calculation method with dislocations pinned at the surface ($\gamma_s \rightarrow \infty$). In these results, the discrepancy between the FEM and Lothe methods is more pronounced and varies with void size and spacing. The largest discrepancy exists for $D = 50b$, $C = 125b$, where τ_c using the Lothe approximation is twice the corresponding value using FEM. This large disparity in τ_c can be attributed to the different conditions required for the dislocation to move along the void surface when the dislocation is pinned at the surface. These conditions are illustrated in Fig. 5 for the void configuration $D = 500b$, $C = 1250b$. Under these circumstances, the dislocation is initially pinned at $x = 0$ with applied stress $\sigma_{xy}^{ext} = 24$ MPa, below τ_c for both image force methods. Since the dislocation cannot glide along the surface, the only way to move along the void periphery is for the dislocation to bow-out until it intersects the surface farther along the void. The thick red line in Fig. 5 indicates the equilibrium configuration using the Lothe approximation. Here, we observe that σ_{xy}^{ext} is insufficient for the dislocation to reach the tangent condition and the dislocation remains pinned at $x = 0$. The thin blue lines labeled (1) through (3) correspond to snapshots of the dislocation evolution when FEM image forces are applied under the same external loading. Line (1) corresponds to the point where the upper end of the dislocation is tangent to the surface, best illustrated in the insert to Fig. 5. Despite the small bow-out of the entire dislocation arm, the attractive image forces have pulled the dislocation towards the surface. From line (2) we observe the point at which the peak bow-out matches that from the Lothe simulation. Due to the attractive image forces pulling the dislocation towards the surface and along the void periphery, the radius of curvature is larger in the simulation with FEM image forces. The larger radius of curvature allows the dislocation to bow-out farther under the
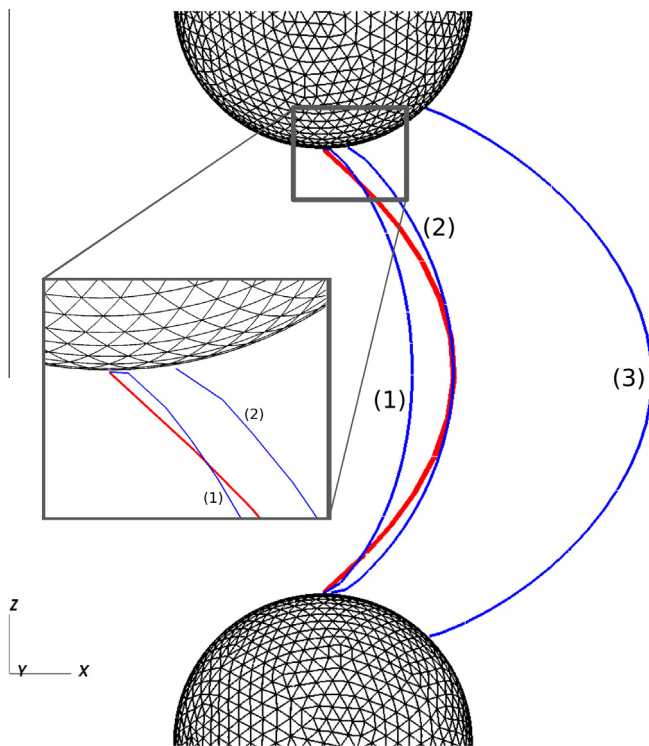
same applied stress. Image forces will then continue to pull the dislocation into the surface, pushing the dislocation even farther along the void periphery. As a result, we demonstrate in line (3) that the equilibrium configuration with FEM image forces has a significantly larger bow-out. In addition, the distance between the ends of the dislocation line is longer since the dislocation has been able to move along the void periphery. Similar to a Frank-Read source, the larger distance between ends will lower the critical stress to reach the instability point. This mechanism of dislocation motion on the surface is only captured when computing image forces on the entire dislocation, whereas the Lothe approximation only accounts for forces at the dislocation-surface intersection point.

Comparing the data represented by empty and solid squares in Fig. 4, we observe the effect of surface mobility with the Lothe approximation for image forces. Similar to the results of Scattergood and Bacon, we note that adding resistance to glide on the surface causes τ_c to align on a single straight line for all void configurations. However, one noteworthy discrepancy between our results and those of Scattergood and Bacon is that our values of τ_c nearly fall along the line for Orowan stress ($\Delta = 0.7$) when surface glide is restricted. In contrast, Scattergood and Bacon find that voids become harder obstacles than impenetrable inclusions with increasing resistance to glide on the surface. Their explanation for this behavior is that the attractive dipole interaction between the dislocation lines is weaker in the case of voids since the trailing Orowan loop is not present. Our results, however, suggest that the upper limit of τ_c for the Lothe approximation is similar to that of Orowan looping. In both cases, the mechanism for dislocation bypass occurs when the dislocation at channel width L reaches the instability point of being tangent to the surface. The slight increase in τ_c for voids, relative to the Orowan stress could be due to the differences in dipole interactions, as suggested by Scattergood and Bacon, but the effect appears to be much smaller than originally reported.

Finally, the comparison of the data represented by the empty and solid triangles in Fig. 4 demonstrates the effect of surface mobility when full image forces are taken into account by means of FEM. For small C, the surface mobility has no effect on τ_c. But, as C increases, the difference between surface mobilities becomes larger. Further work is required to determine why surface mobility only affects τ_c for large void spacing.

In this section, we find that τ_c decreases by as much as a factor of two when image forces are accurately accounted for by FEM. The agreement between the FEM-only and combined FEM plus Lothe methods, shown in Section 3.1, suggests that the difference in τ_c between Lothe and FEM is not due to errors in the force value obtained with the Lothe approximation. Instead, it is due to the fact that image forces on the rest of the dislocation line are ignored. We also find that the effect of dislocation mobility along the surface is insignificant for small void spacing but increases with void spacing when image forces are computed via FEM.

3.3. Stress concentrations

When the external load σ_{xy}^{ext} is applied, stress concentrations form around the voids. In previous studies to determine τ_c for both voids[19] and impenetrable obstacles [18], the stress concentrations around the obstacles have not been accounted for. Through our FEM coupling, the effect of these stress concentrations can be directly incorporated.

In Fig. 6, we compare the values of τ_c with and without the stress concentrations. For simplicity, we only present the results using FEM image forces with $\gamma_s = 0$. However, the results and conclusions are consistent across all combinations of image force
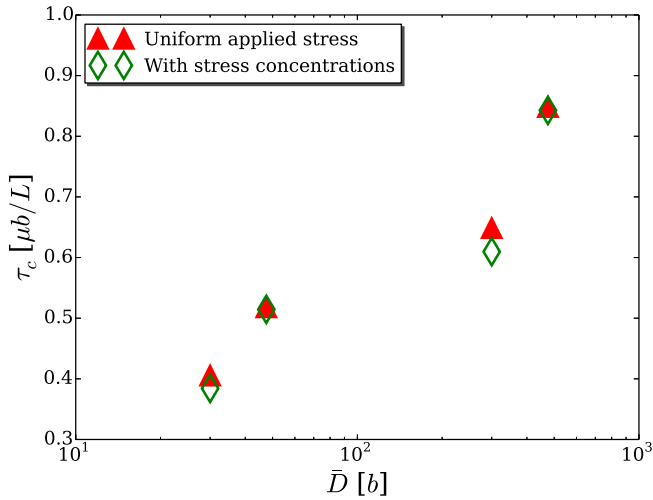

Fig. 5. Comparison of dislocation evolution with $\sigma_{xy}^{ext} = 24$ MPa between Lothe approximation (red line) and FEM (blue lines) for image forces. Dislocation is initially pinned at $x = 0$. Void configuration corresponds to $D = 500b$, $C = 1250b$. (For interpretation of the references to colour in this figure legend, the reader is referred to the web version of this article.)

Fig. 6. Normalized τ_c as a function of void size and spacing illustrating the effect of stress concentrations. Image forces were computed using FEM and dislocations were free to move along the voids surface.

Fig. 8. Normalized τ_c as a function of void size and spacing. All simulations use FEM to compute image forces and include stress concentrations. Surface mobilities are labeled accordingly. The straight lines correspond to Eq. (1) with the values of the fitted coefficient Δ indicated in the legend.

calculation method and surface mobility. The effect of stress concentrations is found to be insignificant for larger values of C/D ($\bar{D} = 47.5$ and 475). This result is consistent with the stress field shown in Fig. 7a, where the effect of the stress concentrations is negligible throughout most of the domain. For lower values of C/D, we observe a 6% drop in τ_c, suggesting that, while there is an effect of the stress concentrations when voids are close together, the effect is small. Again, these results are consistent with the stress contour in Fig. 7b, where the stress concentrations increase the resolved shear stress by only 5–10% in most of the simulation domain. While these results suggest that including the effects due to stress concentrations are not significant in determining the strength of voids as obstacles to dislocation glide, we note that stress concentrations have been shown to play an important role in controlling dislocation evolution around voids such as dislocation nucleation [32,33] and cross-slip [26].

3.4. Void strength model

Having determined the effect of image stress, surface mobility, and stress concentrations on τ_c, we introduce a new model for the
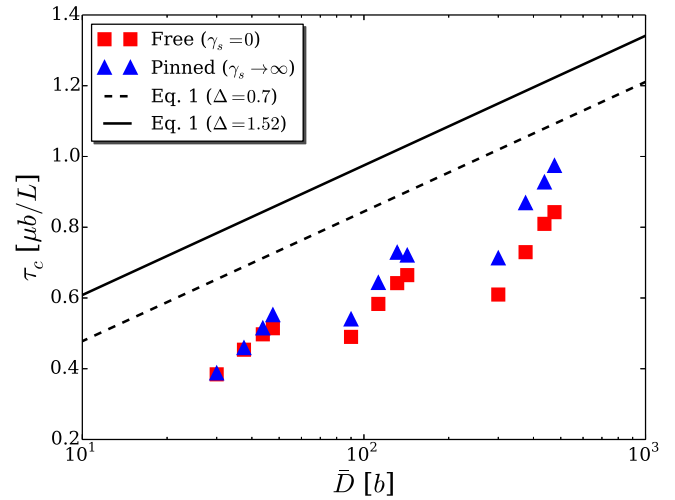
obstacle strength of voids. Our parameter space of void sizes and spacings is increased to include all configurations in Table 1. Image forces are incorporated via the combined FEM with Lothe method with an FEM element size on the void surface of $D/10$. This setup has been shown to be sufficient for mesh convergence in Section 3.1. In order to determine the upper and lower bounds on how surface mobility affects τ_c, we perform simulations with dislocations which are free to glide along the surface ($\gamma_s = 0$) and with dislocation pinned on the surface ($\gamma_s \to \infty$). Stress concentrations are also included.

The normalized value of τ_c for each void configuration is included in Fig. 8 along with Eq. (1) for impenetrable inclusions ($\Delta = 0.7$) and voids ($\Delta = 1.52$). As observed in Section 3.2, our results reveal that Eq. (1) significantly overestimates τ_c, especially when $\Delta = 1.52$. Furthermore, our results do not fall onto a single straight line, suggesting that the normalization of τ_c by $\mu b/L$ does not accurately represent the relationship between τ_c, D, and L. The model of Bacon, Kocks, and Scattergood [18] developed for impenetrable objects (Eq. (1) with $\Delta = 0.7$) correctly predicts the dependence of the obstacle strength on $\mu b/L$ since the instability occurs when the width of the dislocation is equal to L. However, as
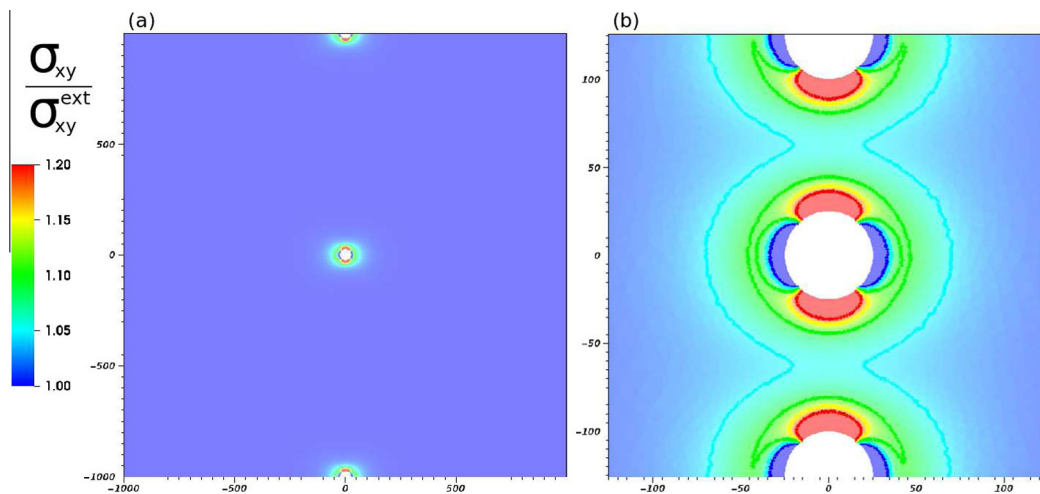

Fig. 7. Stress contours along the $y = 0$ plane, showing areas of increased shear stress (σ_{xy}) relative to the far field loading (σ_{xy}^{ext}). σ_{xy} is the only component of stress responsible for Peach–Koehler forces on the glide plane.
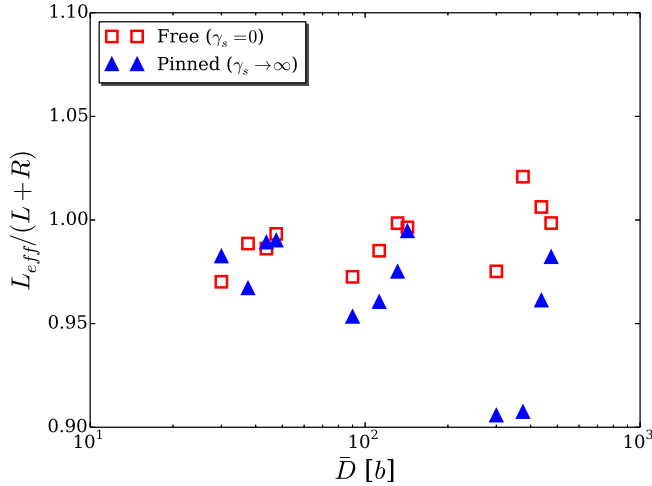
Fig. 9. Comparison of length of the dislocation arm at instability point (L_{eff}) to ($L + R$) for all void configurations.
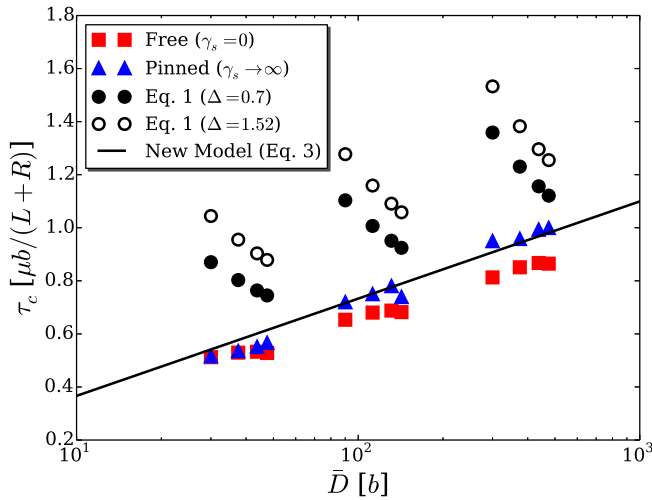

Fig. 10. τ_c, re-normalized by $\mu b/(L + R)$ as a function of void size and spacing. All simulations use FEM to compute image forces and include stress concentrations. Surface mobilities are labeled accordingly. The circles correspond to Eq. (1) with the values of the fitted coefficient Δ indicated in the legend. The solid line corresponds to the new model presented in Eq. (3).

illustrated in Fig. 5, this instability point occurs when the dislocation width is greater than L in the case of voids. As shown schematically in Fig. 1, we define the width of the dislocation arms at the instability point to be L_{eff}, where the instability point is approximated as the equilibrium configuration with $\sigma_{xy}^{ext} = 0.99\tau_c$.

In our simulations, we find that the average value of L_{eff} is approximately $L + R$ where R is the void radius. In Fig. 9, we compare the computed value of L_{eff} with $L + R$ and show that $L_{eff} \approx L + R$ for all void configurations and for both types of surface mobilities. The only configurations where the difference between the compute L_{eff} and $L + R$ is more than 5% are $D = 500b$, $C = 1250b$ and $D = 500b$, $C = 2000b$. However, L_{eff} is still within 10% of $L + R$ in these configurations. By re-normalizing τ_c by $\mu b/(L + R)$ in Fig. 10, we show that τ_c falls on a straight line, with slope approximately $(2\pi)^{-1}$, for all void configurations. Given these findings, a modified equation for the obstacle strength of voids can be expressed as

$$\tau_c = \frac{\mu b}{2\pi(L + R)} \ln\left(\frac{\bar{D}}{b}\right) \qquad (3)$$

We note that $\bar{D}$ is still calculated using the value of L. However, we find the effect of replacing L with $L + R$ to be insignificant on the value of $\ln(\bar{D}/b)$. We also emphasize that no fitted coefficients, such as the Δ term in Eq. (1), are employed in this model. Eq. (3) is represented in Fig. 10 as the solid line and is in excellent agreement with our simulation results when the dislocations are pinned at the surface. In simulations with the dislocations free to move along the surface, we observe that the model diverges from the results with increasing $\bar{D}$. However, Eq. (3) remains within 15% of the computed values for all void configurations and is able to capture the correct dependence on void size and spacing.

While explicitly validating the bypass strength of void arrays is beyond current experimental capabilities, a number of MD simulations have been performed which can be used for comparison with both previous models and our results. Some atomistic simulations have compared favorably with the trends predicted by Eq. (1) [5,6,34]. However, in many of these simulations dislocation climb or cross-slip have been observed, which have been shown to alter the depinning mechanisms and increase τ_c [35]. The void bypass models presented in this article, as well as in Scattergood and Bacon, explicitly neglect these mechanisms. Therefore, any correlation with MD simulations that includes climb or cross-slip should be serendipitous rather than an indication of the accuracy of the model. Other MD results have indicated that Eq. (1) can significantly overestimate the strength of voids as obstacles to dislocation motion [3,7,36]. While Bitzek and Gumbsch [7] have shown that inertial effects are one factor that reduces τ_c, our results suggest that image forces also contribute to the reduction in τ_c, compared to Eq. (1). The inclusion of cross-slip, climb, and inertia into the DD model is needed in order to capture the depinning mechanisms observed in many MD simulations. Inclusion of these phenomena may also explain the strong temperature dependence of τ_c observed in MD studies [35,34]. In addition, MD simulations with larger void diameters are needed for comparisons at length scales better suited for DD simulations.

4. Conclusions

In this article, we employ a coupled DD-FEM simulator to determine the strength of voids as obstacles to dislocation glide. Following the classical model of Scattergood and Bacon, an infinite dislocation is driven towards a one-dimensional array of voids as to quantify the critical bypass stress. Many of the approximations made in Scattergood and Bacon [19] with regards to the treatment of the voids' free surfaces are re-examined with the help of a more accurate method for computing image forces. The main conclusions of this article are as follows:

1. The Lothe approximation for image forces causes a significant overestimation of the critical bypass stress, τ_c. This is due primarily to the fact that the Lothe approximation only includes the image force acting on the dislocation at the surface. The FEM solution for image forces includes the interaction with the entire dislocation line, which pulls the dislocation past the void. This effect is strongest when dislocations are unable to glide along the void surface due to high surface energy.
2. The effects of stress concentrations around the void are not significant. A small reduction in τ_c of approximately 6% is observed at high void densities while no effect is observed at lower void densities.
3. Employing a combination of FEM solution and Lothe approximation to compute image forces provides the same accuracy with coarser FEM element sizes. This provides substantial reduction in the computational expense of the image force calculation. However, we emphasize that this combined

method is only proven to be equivalent for quasi-static simulations and may not be true for dynamic simulations.
4. Our simulation results can be systematically characterized by a new model for τ_c which eliminates many of the approximations in the model of Scattergood and Bacon. The new model predicts a significantly lower critical stress for dislocations to bypass an array of voids and suggests that voids are weaker obstacles to dislocation glide than impenetrable inclusions.

Acknowledgments

References

[1] M. Makin, F. Minter, S. Manthorpe, The correlation between the critical shear stress of neutron irradiated copper single crystals and the density of defect clusters, Phil. Mag. 13 (124) (1966) 729–739.
[2] P. Manusmare, H.L. Leighly JR., Void-strengthening in aluminum and its nature, Acta Metall. 24 (1976) 1047–1052.
[3] A. Simar, H.-J. Voight, B. Wirth, Molecular dynamics simulations of dislocation interaction with voids in nickel, Comput. Mater. Sci. 50 (2011) 1811–1817.
[4] Y. Osetsky, D. Bacon, Comparison of void strengthening in fcc and bcc metals: large-scale atomic-level modelling, Mater. Sci. Eng. A 400 (2005) 374–377.
[5] Y. Osetsky, D. Bacon, V. Mohles, Atomic modelling of strengthening mechanisms due to voids and copper precipitates in α-iron, Phil. Mag. 83 (2003) 3623–3641.
[6] D. Terentyev, D. Bacon, Y. Osetsky, Interaction of an edge dislocation with voids in α-iron modelled with different interatomic potentials, J. Phys. Condens. Matter 20 (2008) 445007.
[7] E. Bitzek, P. Gumbsch, Dynamic aspects of dislocation motion: atomistic simulations, Mater. Sci. Eng. A 400–401 (2005) 40–44.
[8] S.H. Haghighat, M. Fivel, J. Fikar, R. Schaeublin, Dislocation–void interactions in fe: a comparison between molecular dynamics and dislocation dynamics, J. Nucl. Mater. 386–388 (2009) 102–105.
[9] Z. Yang, S. Watanabe, T. Kato, The irradiation effect of a simultaneous laser and electron dual-beam on void formation, Sci. Rep. 3 (2013) 1–6.
[10] J. Brimhall, B. Mastel, Voids in neutron irradiated face centered cubic materials, J. Nucl. Mater. 29 (1969) 123–125.
[11] J. Yue, W. Funsten, R. Taylor, Stress induced voids in aluminum interconnects during ic processing, in: Reliability Physics Symposium, 1985. 23rd Annual, IEEE, 1985, pp. 126–137.
[12] N. Forouzanmehr, N. Nili-Ahmadabadi, On the atomic force microscopy characterization of void evolution in severely plastic deformed pure iron, in: IOP Conference Series: Materials Science and Engineering, vol. 63, IOP Publishing, 2014, p. 012149.
[13] X. Gong, T. Anderson, K. Chou, Review on powder-based electron beam additive manufacturing technology, Manufact. Rev. 1 (2014) 2.
[14] S. Queyreau, G. Monnet, B. Devincre, Orowan strengthening and forest hardening superposition examined by dislocation dyanmics simulations, Acta Mater. 58 (2010) 5586–5595.
[15] A. Arsenlis, M. Rhee, G. Hommes, R. Cook, J. Marian, A dislocation dynamics study of the transition from homogeneous to heterogeneous deformation in irradiated body-centered cubic iron, Acta Mater. 60 (2012) 3748–3757.
[16] M. Krug, Z. Mao, D. Seidman, D. Dunand, Comparison between dislocation dynamics model predictions and experiments in precipitation-strengthened al–li–sc alloys, Acta Mater. 79 (2014) 382–395.
[17] E. Orowan, Symposium on internal stresses in metals and alloys, Inst. Metals (London) (1948) 451.
[18] D. Bacon, U. Kocks, R. Scattergood, The effect of dislocation self-interaction on the Orowan stress, Phil. Mag. 28 (1973) 1241–1263.
[19] R. Scattergood, B. Bacon, The strengthening effect of voids, Acta Metall. 30 (1982) 1665–1677.
[20] J. Crone, P. Chung, K. Leiter, J. Knap, S. Aubry, G. Hommes, A. Arsenlis, A multiply parallel implementation of finite element-based discrete dislocation dynamics for arbitrary geometries, Modell. Simul. Mater. Sci. Eng. 22 (2014) 035014.
[21] K. Leiter, J. Crone, J. Knap, An algorithm for massively parallel dislocation dynamics simulations of small scale plasticity, J. Comput. Sci. 4 (2013) 401–411.
[22] A. Arsenlis, W. Cai, M. Tang, M. Rhee, T. Oppelstrup, G. Hommes, T. Pierce, V. Bulatov, Enabling strain hardening simulations with dislocation dynamics, Modell. Simul. Mater. Sci. Eng. 15 (2007) 553–595.
[23] E. van der Giessen, A. Needleman, Discrete dislocation plasticity: a simple planar model, Modell. Simul. Mater. Sci. Eng. 3 (1995) 689–735.
[24] W. Cai, A. Arsenlis, C. Weinberger, V. Bulatov, A non-singular continuum theory of dislocations, J. Mech. Phys. Solids 54 (2006) 561–587.
[25] D. Weygand, L. Friedman, E.V. der Giessen, A. Needleman, Aspects of boundary-value problem solutions with three-dimensional dislocation dynamics, Modell. Simul. Mater. Sci. Eng. 10 (2002) 437–468.
[26] L. Munday, J. Crone, J. Knap, The role of free surfaces on the formation of prismatic dislocation loops, Scr. Mater. 103 (2015) 65–68.
[27] J. Lothe, The image force on dislocations at free surfaces-comments on the concept of line tension, in: Fundamental aspects of dislocation theory, in: J.A. Simmons, R. deWit, R. Bullough (Eds.), vol. 319, National Bureau of Standards, 1970, pp. 11–22.
[28] C. Weinberger, Dislocation drag at the nanoscale, Acta Mater. 58 (2010) 6535–6541.
[29] E. Bitzek, P. Gumbsch, Atomistic study of drag, surface and inertial effects on edge dislocations in face-centered cubic metals, Mater. Sci. Eng. A 387–389 (2004) 11–15.
[30] M. Tang, G. Xu, W. Cai, V. Bulatov, Dislocation image stresses at free surfaces by the finite element method, Materials Research Society Proceedings 795.
[31] M. Tang, W. Cai, G. Xu, V. Bulatov, A hybrid method for computing forces on curved dislocations intersecting free surfaces in three-dimensional dislocation dynamics, Modell. Simul. Mater. Sci. Eng. 14 (2006) 1139–1151.
[32] A. Pohjonen, F. Djurabekova, K. Nordlund, A. Kuronen, S. Fitzgerald, Dislocation nucleation from near surface void under static tensile stress in cu, J. Appl. Phys. 110 (2011) 023509.
[33] D. Hull, D. Bacon, Introduction to Dislocations, Elsevier Ltd., 2011.
[34] Y. Osetsky, D. Bacon, Atomic-scale mechanisms of void hardening in bcc and fcc metals, Phil. Mag. 90 (2010) 945–961.
[35] T. Hatano, T. Kaneko, Y. Abe, H. Matsui, Void-induced cross slip of screw dislocations in fcc copper, Phys. Rev. B 77 (2008) 064108.
[36] L. Xiong, S. Xu, D. McDowell, Y. Chen, Concurrent atomistic–continuum simulations of dislocation–void interactions in fcc crystals, Int. J. Plast. 65 (2015) 33–42.